

# Speed of sound measurements and mixing characterization of underexpanded fuel jets with supercritical reservoir condition using laser-induced thermal acoustics

S. Baab<sup>1</sup> · F. J. Förster<sup>1,2</sup> · G. Lamanna<sup>1</sup> · B. Weigand<sup>1</sup>

Received: 1 July 2016 / Revised: 4 September 2016 / Accepted: 11 September 2016 / Published online: 22 October 2016  
© Springer-Verlag Berlin Heidelberg 2016

**Abstract** The four-wave mixing technique laser-induced thermal acoustics was used to measure the local speed of sound in the farfield zone of extremely underexpanded jets. *N*-hexane at supercritical injection temperature and pressure (supercritical reservoir condition) was injected into quiescent subcritical nitrogen (with respect to the injectant). The technique's capability to quantify the nonisothermal, turbulent mixing zone of small-scale jets is demonstrated for the first time. Consistent radially resolved speed of sound profiles are presented for different axial positions and varying injection temperatures. Furthermore, an adiabatic mixing model based on nonideal thermodynamic properties is presented to extract mixture composition and temperature from the experimental speed of sound data. High fuel mass fractions of up to 94 % are found for the centerline at an axial distance of 55 diameters from the nozzle followed by a rapid decay in axial direction. This is attributed to a supercritical fuel state at the nozzle exit resulting in the injection of a high-density fluid. The obtained concentration data are complemented by existing measurements and collapsed in a similarity law. It allows for mixture prediction of underexpanded jets with supercritical reservoir condition provided that nonideal thermodynamic behavior is considered for the nozzle flow. Specifically, it is shown that the fuel concentration in the

farfield zone is very sensitive to the thermodynamic state at the nozzle exit. Here, a transition from supercritical fluid to subcritical vapor state results in strongly varying fuel concentrations, which implies high impact on the mixture formation and, consequently, on the combustion characteristics.

## 1 Introduction

Characterization of fluid injection into a gaseous environment is of paramount interest for virtually all combustion-based energy conversion concepts. Particularly for internal combustion engines and gas turbines, confident knowledge of the fuel/air mixture preparation is crucial. Fuel is commonly injected in a liquid state and atomizes during the process. Vaporization of small droplets and subsequent mixing of fuel vapor with ambient air results in a combustible mixture. Here, the local mixture composition and temperature are known to influence the engine efficiency as well as pollutant formation significantly (Idicheria and Pickett 2007; Bougie et al. 2005; Kiefer et al. 2008). Although this clearly illustrates the need for detailed experimental data, quantitative measurements within the vapor region remain an inherently challenging task. High injection velocities in combination with a small nozzle geometry lead to highly turbulent jet disintegration phenomena on a scale of a few millimeters.

Concentration and temperature data within fuel/gas mixtures are usually obtained with nonintrusive optical techniques such as Rayleigh/Mie (Espey et al. 1997; Su et al. 2010; Idicheria and Pickett 2007), LIF/LIEF (Wolff et al. 2007; Cruyningen et al. 1990; Payri et al. 2006), Raman (Weigl et al. 2006; Grünefeld et al. 1994; Taschek et al. 2005) and CARS (Weigl et al. 2006; Seeger et al. 2003; Chai et al. 2007). In addition to these techniques,

✉ S. Baab  
steffen.baab@itlr.uni-stuttgart.de

F. J. Förster  
felix.foerster@physics.ox.ac.uk

<sup>1</sup> Institute of Aerospace Thermodynamics (ITLR), University of Stuttgart, Pfaffenwaldring 31, 70569 Stuttgart, Germany

<sup>2</sup> Atomic and Laser Physics Clarendon Laboratory, University of Oxford, Parks Road, Oxford OX13PU, UK

laser-induced thermal acoustics (LITA), also known as laser-induced grating spectroscopy (LIGS), has emerged as an effective and robust alternative for quantitative measurements in gaseous mixtures.

LITA is a nonintrusive, typically seedless, point-measurement technique that generally classifies as four-wave mixing technique. It provides spatially and temporally resolved measurements of the local speed of sound, flow velocity and transport properties. For known species concentration, temperature can be derived from the speed of sound or vice versa. A unique feature of LITA is that data extraction can be realized independently from the signal intensity. In fact, speed of sound and flow velocity are solely found from a frequency analysis of the time-resolved signal. This is especially beneficial if signal quality is low, e.g. when the measurement is strongly deteriorated by stray light or other negative influences of harsh environmental conditions—a major difficulty for the intensity-based techniques Raman, Rayleigh, LIF and CARS. Furthermore, LITA exhibits a fairly simple calibration procedure performed in a fluid at an arbitrary, but known thermodynamic state rather than at conditions that are close to those expected in the experiment. On the other hand, the established techniques are effectively instantaneous, while relevant time scales for the LITA signal are in the order of a few hundred nanoseconds. Hence, effects with lower characteristic times, e.g. highly nonequilibrium processes, are not resolvable.

Given the individual requirements of a particular application, it remains, however, difficult to assess all techniques universally. With respect to injection studies, a detailed discussion of advantages and disadvantages using LITA in comparison with more established techniques can be found in several publications (Seeger et al. 2006; Kiefer et al. 2008; Williams et al. 2014; Roshani et al. 2013). In these studies, the effectiveness and robustness of LITA have convinced to use it for quantitative mixture characterization with relevance to combustion science.

So, most recently, Williams et al. (2014) applied LITA to determine in-cylinder gas temperatures within an optical GDI engine. Measurements were taken during the compression process prior to ignition, which allowed the assumption of a homogeneous fuel/gas mixture with known composition. The gas temperatures could then be obtained from experimental speed of sound data with excellent precision below 1 %.

The direct mixing zone of fuel and ambient gas, however, generally features an inhomogeneous concentration field. In fact, the local fuel/gas composition is of high interest as it dictates the mixture formation and resulting combustion quality (Idicheria and Pickett 2007).

Consequently, Seeger et al. (2006) and Kiefer et al. (2008) investigated the mixture formation process of

gaseous propane when injected into nitrogen. Injection and chamber pressure were fixed to 13 and 3 bar, whereas nearly isothermal mixing was assured by choosing the injection and chamber temperature to 330 and 345 K, respectively. As propane features weak absorption at their excitation wavelength, concentrations could be determined from the intensity ratio of resonant and nonresonant contribution to the LITA signal as it was originally proposed by Schlamp and Sobota (2002). For the aforementioned studies, this procedure was limited to propane mole fractions below 3 % as purely resonant signals were obtained beyond this concentration. Due to the nearly isothermal mixing process, however, mole fractions above 3 % could be derived directly from the speed of sound relation for ideal gases instead of the intensity ratio.

Roshani et al. (2013) explored the application of LITA for nonisothermal mixture formation in a flash-boiling propane jet injected into nitrogen. Again, the resonant/nonresonant intensity ratios could be used as the obtained propane concentrations were within 1 % in volume. By assuming this ratio as constant over the relevant temperature range, mixture temperatures were calculated based on the found concentration and the measured speed of sound using the ideal gas relation. This assumption, however, limits the approach to small temperature differences within the mixture and low injectant concentrations as present in their experiments.

Up to now, LITA measurements have not yet been realized in mixing zones with high fuel concentration and non-uniform temperature fields although this is clearly desirable from an engineering point of view. A good example is the injection of fuel at supercritical reservoir condition (i.e. supercritical injection temperature and pressure), which recently has become of high interest in combustion technology. For diesel engines, it is a promising approach to increase the engine efficiency with a simultaneous reduction in emission (Antiescu et al. 2009; Tavlarides and Antiescu 2009). Furthermore, modern gas turbine concepts and hypersonic flight vehicles rely on the cooling of thermally stressed aircraft components using an endothermic fuel as heat sink, which can also lead to supercritical injection temperatures (and pressures) (Edwards 1993; Wu et al. 1996). Physical implications of near-critical mixing at high pressure, usually accompanied by highly nonideal thermodynamic transport processes, are object to several recent research activities (Dahms and Oefelein 2015; Borghesi and Bellan 2015; Segal and Polikhov 2008; Falgout et al. 2016) and will not be addressed in detail here.

Based on this brief outline, the objective of the present paper is to investigate surrogate fuel jets at supercritical reservoir conditions injected into a subcritical atmosphere. It distinguishes this work from existing studies in multiple aspects. For the first time, LITA was applied to jet mixing

zones with both significant concentration and temperature gradients. The turbulent farfield zone was analyzed for an extremely underexpanded jet with small spatial scale. Its flow field properties represent very harsh conditions for LITA measurements as high shear rates and turbulent mixing are known to disturb the signal formation and, hence, data acquisition (Kuehner et al. 2010). Still, quantitative speed of sound profiles were obtained at several axial planes downstream of the nozzle. In addition, the injection temperature was systematically varied to allow for a detailed characterization of the mixing process. A novel framework to extract mixture composition and temperature based on experimental speed of sound data is provided using a mixing model with nonideal thermodynamic properties. The resulting concentration distributions are unified with existing experimental data for similar injection conditions (Wu et al. 1999) by means of a similarity law. Under proper consideration of nonideal thermodynamic behavior, this allows for the farfield mixture characterization of underexpanded jets at supercritical injection pressure and temperature.

This study demonstrates the feasibility of LITA to investigate small-scale jet mixing processes, which paves the way to obtain more quantitative data on mixture formation under challenging thermo- and aerodynamic conditions. Furthermore, the obtained quantitative data may serve as reference for validation of numerical codes as well as the design of future combustion systems.

## 2 Experimental facility and measurement technique

### 2.1 Test chamber and injection system

The jet experiments were performed in a cylindrical constant-volume chamber ( $V \approx 4 \times 10^{-3} \text{ m}^3$ ). Chamber pressure  $p_{\text{ch}}$  was measured with a piezoresistive sensor (Keller PA-21Y, 0.025 % uncertainty), while two K-type thermocouples provided the temperature  $T_{\text{ch}}$  within  $\pm 1 \text{ K}$ . The test gas in the chamber was exchanged after a maximum of 10 injections to avoid accumulation of the injectant within the chamber atmosphere. Furthermore, it was taken care that  $T_{\text{ch}}$  could adapt to ambient temperature prior to the next set of experiments and did not change during an injection sequence. Two quartz windows (Schott Lithosil TM Q1) provided optical access into the chamber. A common rail injection system is integrated into the front side end wall so that the axis of injector nozzle and cylinder coincide. The magnetic-valve injector is commercially distributed by Robert Bosch AG. A custom nozzle with a single straight-hole of diameter  $D = 0.236 \text{ mm}$  and length  $L = 1 \text{ mm}$  (i.e.  $L/D \approx 4.2$ ) was used. Two temperature-controlled heater

cartridges are attached to the injector body and tip to pre-heat the fluid prior to injection. The temperature calibration of the injection system has been performed in Stotz (2011) and was verified prior to this campaign. The uncertainty of injection temperature  $T_{\text{inj}}$  is considered to be within  $\pm 2 \text{ K}$ .

### 2.2 Laser-induced thermal acoustics (LITA)

#### 2.2.1 Principle

Two beams of a short-pulse laser source (excitation laser) are crossed to modulate the density of the test medium within the measurement volume. The resulting spatially periodic perturbation with fringe spacing  $\Lambda$  scatters light of a third input wave originating from a second laser source (interrogation laser) into the coherent LITA signal beam from which physical properties of the test medium are derived.

In gas phases, the grating formation is dominated by two optoacoustic effects, namely electrostriction (non-resonant) and thermalization (resonant). Rapid forcing of the test medium by the applied electric field results in two counter-propagating, plane acoustic waves. In case of resonant grating excitation—as it is present in this study—an additional thermal grating is generated. Light scattered from these structures resolves the temporal evolution of all present waves as function of the gas properties. Consequently, the LITA signal is observed as damped oscillation with frequency  $\Omega_0$ , which is proportional to the local speed of sound in the test medium. In addition, flow velocity and transport properties may also be derived from the characteristic LITA signal shape.

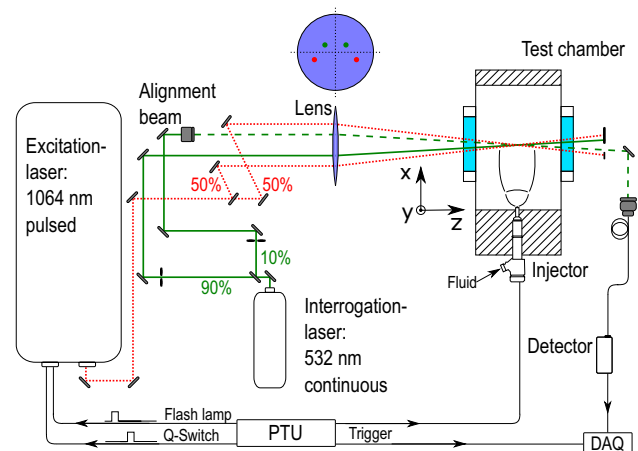


**Fig. 1** Experimental setup of LITA measurements in fuel jets

### 2.2.2 Optical setup

The optical arrangement is illustrated in Fig. 1 and was adapted from the setup described in Förster et al. (2015). For the excitation beam, a pulsed Nd:YAG laser (Continuum Powerlite 8010,  $\tau_{\text{pulse}} = 7$  ns FWHM, 30 GHz linewidth) is used at its first fundamental output wavelength of  $\lambda = 1064$  nm. The interrogation beam originates from a continuous laser source at 532 nm (Coherent Verdi V8, 5 MHz linewidth). All beams are aligned parallel to each other using the mirror system in Fig. 1. The focusing lens has a focal length of 700 mm, which results in a  $3^\circ$  crossing angle of the excitation beams.

The signal beam is spatially and spectrally filtered before it is directed onto a photo detector (Thorlabs APD110) via a single-mode fiber. The output power of the excitation laser was kept constant at 50 mJ for all experiments, while the power of the interrogation laser ranged between 0.25 and 2 W to ensure sufficient signal-to-noise ratios for all injection conditions. The laser and detection system are synchronized with the injection system via a programmable timing unit. The trigger logic generates an intermediate laser pulse within the nominal laser repetition rate relative to a distinct event in time, i.e. the injector activation. Similar to the approach described in Förster et al. (2015), it allows to take measurements at a fixed time of 1.6 ms after start of injection.

Given the small scale of the investigated jets, precise alignment of the measurement volume relative to the mixing zone is an important aspect. Therefore, the paths of the excitation and interrogation beams were tracked by traversing a CCD chip through the intersection region, an approach suggested by Tedder et al. (2008) and Roshani et al. (2013) for CARS and LITA systems, respectively. The CCD chip was mounted on a three axes traverse that featured the same coordinate system as test chamber and jet. This arrangement ensured that all involved beams intersected at the desired location. The intersection region of the excitation beams was of ellipsoidal shape with a diameter of approximately  $200 \mu\text{m}$  and  $<8$  mm in length. Note that this represents the worst-case approximation of the measurement volume as the interrogation beam only partially penetrates the excited region. Consequently, good radial (and axial) resolution of the jets—whose characteristic dimensions typically comprise several nozzle diameter ( $D = 236 \mu\text{m}$ )—is provided, whereas the signal contribution is partly averaged in beam direction. The spatial increment between two measurement positions was accurately determined in both axial and radial direction using the CCD chip.

### 2.2.3 Frequency determination scheme

In the time domain, LITA signals are typically observed as damped sinusoids with frequency  $\Omega_0$  that can be determined, e.g. via spectral frequency analysis (Förster et al. 2015). This works best if a reasonable number of oscillations in sufficient quality are detected and the signal intensity decays to zero within the grating lifetime.

Within this study, however, recorded signals demanded for an alternative frequency extraction scheme. As the injected fluid may feature a higher density than its surrounding gas, an inhomogeneous density field along the beam path-lengths might be present. Density-gradient-based beam steering then deteriorates the LITA signal resulting in a nonzero intensity even when no grating is excited. The same steering effect can also cause an alteration of the crossing angles that contributes to the overall uncertainty of the measurement. Additionally, high shear rates within the measurement volume and turbulent time scales comparable to the LITA lifetime disrupt the fringe pattern, which significantly increases the signal decay rate (Kuehner et al. 2010). Consequently, the number of detectable oscillations decreases, whereas a premature dissipation of the grating is likewise possible. As a consequence, the frequency detection scheme must accommodate a low number of oscillations in combination with irregularly shaped signals.

In Fig. 2, a typical normalized LITA signal taken in the farfield mixing zone of an underexpanded jet is illustrated. Only three distinct oscillations can be identified, indicating a fast signal decay due to the aforementioned reasons. For the jet experiments considered here, typically between two

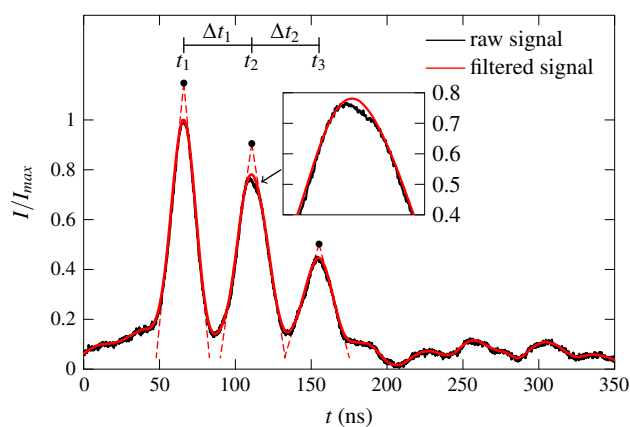


**Fig. 2** Exemplary LITA signal including filtered signal and triangulation scheme for frequency determination

and five oscillations were processable. Refraction of the interrogation beam, induced by the inhomogeneous flow field, causes normalized intensities  $I/I_{\max} > 0$  prior to and after the grating lifetime. It is believed that this effect also translates into the often irregularly shaped peaks (e.g. second peak in Fig. 2).

An individual detection of the oscillation periods  $\Delta t_i = t_{i+1} - t_i$  between distinct signal peaks is considered to be superior to a FFT as the latter performs best when it is applied to periodic signals of symmetric shape and a sufficient number of periods. As manual selection of the peak locations is prone to error due to the signal irregularities, a different approach was developed here. First, a Savitzky–Golay filter (red curve) was applied to smooth the distribution, and the characteristic time  $t_i$  of an individual peak was determined by the intersection of tangents on rising and falling edge defined by a gradient criterion. The LITA frequency  $\Omega_0$  is calculated by averaging the reciprocal periods according to  $\Omega_0 = \frac{1}{N} \sum_{i=1}^N \frac{1}{\Delta t_i}$ , with  $N + 1$  processable peaks. Note that the method does not rely on the evaluation of distinct signal peaks but is based on the dynamics in the rise and fall period, which makes it robust against aforementioned nonidealities and the shape of the oscillation peaks. For fast-decay signals with asymmetric flanks due to different fall and rise times, the approach may result in systematically higher frequencies. For the present application, it was however found that this effect alters the accuracy of the technique by  $< 1\%$ . Further validation was obtained for slow-decay signals with more than 10 oscillations, where FFT and theoretical model fits feature the best accuracy. In comparison with these established methods, the chosen approach yields identical results.

### 2.2.4 Calculation of thermodynamic quantities from LITA data

Once  $\Omega_0$  is obtained from experimental data, the adiabatic speed of sound  $a$  of the fluid (mixture) can be derived. For resonant grating excitation with fringe spacing  $\Lambda$ , it is

$$a = \Omega_0 \Lambda. \tag{1}$$

Typically,  $\Lambda$  is found from frequency measurements in a fluid with known speed of sound. In context of this study, these were performed in pure nitrogen at ambient temperature filled into the chamber described in Sect. 2.1. The

calibration procedure is identical to the one in Förster et al. (2015), where the effect of uncertainties from the calibration is found to be within 1.3 %.

For a mixture of gases in local thermodynamic equilibrium,  $a_{\text{mix}}$  is generally a function of species concentration, temperature and pressure, i.e

$$a_{\text{mix}} = a_{\text{mix}}(\underline{c}, T, p), \tag{2}$$

where  $\underline{c} = (c_i)_{i=1, \dots, M}$  is the mass fraction vector for  $M$  components. Hence, for an isobaric mixing process at known pressure,  $a_{\text{mix}}$  is defined by the local mixture composition and temperature. On the basis of a measured speed of sound  $a_{\text{meas}}$ , either  $T$  can be determined for known  $\underline{c}$  or vice versa. For this, the relation  $a_{\text{mix}}(\underline{c}, T, p) = \sqrt{\gamma_{\text{mix}} R_{\text{mix}} T}$  with  $\gamma_{\text{mix}}$  as the ratio of specific heats and  $R_{\text{mix}}$  the specific gas constant may be used for ideal gas mixtures.

However, if one or more mixture components can not be approximated as ideal gases, this simple relation for  $a_{\text{mix}}$  is not valid anymore. In particular, for fluids close to their saturation state (e.g. dew-point line) and at high pressures (possibly even beyond the critical pressure), incorporation of real fluid behavior is mandatory. High-order equations of state (EOS) in combination with nonlinear mixing rules are then necessary to calculate thermodynamic properties.

## 3 Measurement conditions

*N*-hexane ( $\text{C}_6\text{H}_{14}$ ) jets were injected into a quiescent nitrogen ( $\text{N}_2$ ) atmosphere. A constant injection pressure of  $p_{\text{inj}} = 300$  bar was maintained, whereas injection (or reservoir) temperature  $T_{\text{inj}}$  varied from 554 to 630 K. With respect to the critical values of *n*-hexane ( $T_c = 507.8$  K,  $p_c = 30.34$  bar), the reduced parameters  $p_{\text{inj}}^r = p_{\text{inj}}/p_c$  and  $T_{\text{inj}}^r = T_{\text{inj}}/T_c$  are both supercritical with  $p_{\text{inj}}^r = 9.9$  and  $T_{\text{inj}}^r = 1.09\text{--}1.24$ . The chamber temperature and pressure were chosen constant at  $T_{\text{ch}} = 295$  K ( $T_{\text{ch}}^r = 0.58$ ) and  $p_{\text{ch}} = 2$  bar ( $p_{\text{ch}}^r = 0.07$ ).

Table 1 summarizes the experimental conditions considered in this study. Measurements at the jet centerline ( $y/D = 0$ ) were taken for four  $T_{\text{inj}}$ . Additionally, radial profiles for  $T_{\text{inj}} = 554$  and 630 K were obtained at dimensionless distances from the nozzle exit of  $x/D = 55$  and 80.

The nozzle pressure ratio  $p_{\text{inj}}/p_{\text{ch}}$  remains constant at 150 for all experiments. According to a classification proposed by

**Table 1** Overview of experimental conditions

$T_{\text{inj}}$ (K)	$T_{\text{inj}}^r$	$p_{\text{inj}}$ (bar)	$T_{\text{ch}}$ (K)	$p_{\text{ch}}$ (bar)	Centerline (at $x/D$ )	Radial profile (at $x/D$ )
554	1.09	300	295	2	55;80;110	55;80
577	1.14	300	295	2	55;80;110	–
600	1.18	300	295	2	55;110	–
630	1.24	300	295	2	55;80;110	55;80

**Fig. 3** Exemplary shadowgram of an extremely underexpanded jet including visualization of post-shock state and the first two axial measurement positions

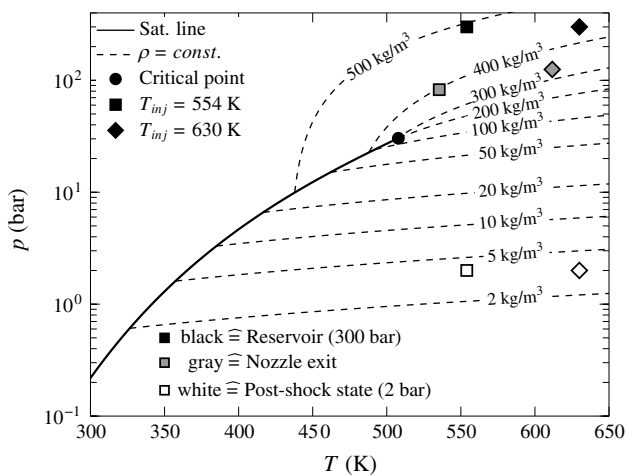
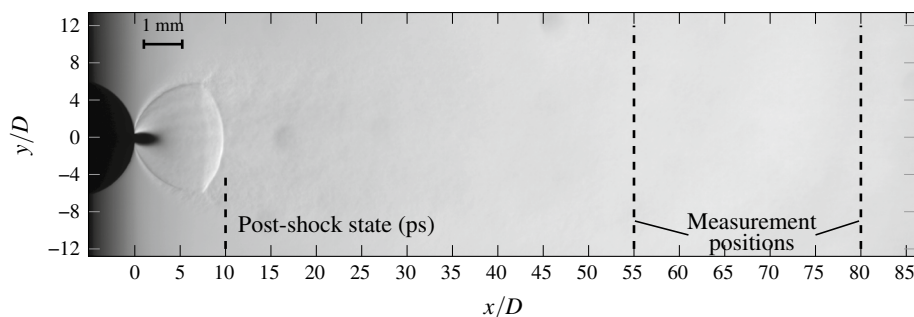


**Fig. 4**  $p$ ,  $T$ -diagram of pure  $n$ -hexane including reservoir conditions as well as nozzle exit and post-shock state

Franquet et al. (2015), ratios  $p_{inj}/p_{ch} \geq 7$  typically lead to very highly (or extremely) underexpanded jets with a single barrel-shaped shock structure to adapt the flow to  $p_{ch}$ . The typical flow pattern is illustrated in Fig. 3 by a representative shadowgram for a jet at  $T_{inj} = 554$  K with  $p_{inj}/p_{ch} = 300$ . Here, a single shock barrel is clearly visible at  $0 \leq x/D < 10$ .

Due to the expanding flow at the nozzle exit, entrainment of  $N_2$  into the interior of the shock barrel can be neglected (Harstad and Bellan 2006). Along the nozzle axis, the flow is facing an approximately normal shock (“Mach disk”) after which the static post-shock pressure  $p_{ps}$  equals  $p_{ch}$ . The immediate post-shock temperature  $T_{ps}$  can be approximated as equal to  $T_{inj}$  (i.e.  $T_{ps} = T_{inj}$ ) (Harstad and Bellan 2006; Ewan and Moodie 1986; Birch et al. 1987).

The mixing characteristics downstream of the Mach disk generally depend upon the initial injection conditions (Molkov 2012). It is, therefore, necessary to classify the thermodynamic regime that is relevant for the expansion process from reservoir to post-shock state. Hence, a  $p$ ,  $T$ -diagram of pure  $n$ -hexane is provided in Fig. 4. The data for saturation line (solid), isochores (dashed) and critical point were taken from NIST REFPROP (Lemmon et al. 2013), which uses a Helmholtz EOS developed by Span

and Wagner (2003) with maximum uncertainties in density and speed of sound of 0.5 and 2 %, respectively.

Reservoir conditions (black) for  $T_{inj} = 554$  and 630 K are illustrated together with the approximated post-shock states (white) at  $p_{ps} = p_{ch} = 2$  bar. An estimation of the thermodynamic state at the nozzle exit (gray) is also included, which was calculated using a one-dimensional flow code based on isentropic flow assumption through the nozzle. This procedure was originally developed by Wu et al. (1996) and applied to the present configuration by Baab et al. (2014).

Both reservoir and nozzle exit conditions are located well within the supercritical fluid regime (i.e.  $p_{inj} > p_c, T_{inj} > T_c$ ) involving liquid-like densities of 300–500  $\text{kg m}^{-3}$  for the flow within the nozzle. In contrast to that, subcritical vapor of significantly lower density is expected for the post-shock state. Note that, due to the vicinity to the critical point, nonideal thermodynamic behavior has to be considered for the characterization of the entire expansion process (provided by the Helmholtz EOS used for  $n$ -hexane).

Downstream of the Mach disk, the  $n$ -hexane jet progressively entrains ambient  $N_2$  that prevents a single-species treatment for state evaluation. In fact, consideration of mixture thermodynamics of the binary  $n$ -hexane/ $N_2$  system is compulsory.

## 4 Results

The results are presented in two parts. Experimental speed of sound data sets are provided at different positions and varying injection temperature. Based on these measurements, concentration and temperature are determined using an adiabatic mixing model based on nonideal fluid properties.

### 4.1 Experimental speed of sound data

To allow for a first interpretation of the measured speed of sound data, it is useful to estimate the possible range for  $a_{meas}$  as a scale of reference. This range is determined by

**Table 2** Speed of sound of pure *n*-hexane and N<sub>2</sub> at relevant temperatures and  $p_{ch} = 2$  bar

$T$ (K)	295	554	577	600	630
$a_{hex}$ (m/s)	–	231.9	237.0	242.0	248.3
$a_{N_2}$ (m/s)	350.4	–	–	–	–

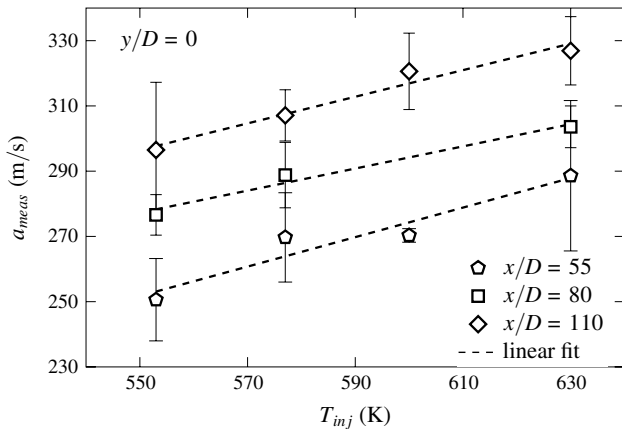


**Fig. 5**  $a_{meas}$  at centerline ( $y/D = 0$ ) for varying  $T_{inj}$  and  $x/D$

$a_{hex}$  (pure *n*-hexane) at  $T_{ps}$  on the one hand, and by  $a_{N_2}$  at chamber condition on the other hand. Table 2 lists the relevant speed of sound data taken from NIST (Lemmon et al. 2013).

It should be noted that the spread in the speed of sound of the mixing components (i.e.  $a_{hex}$  and  $a_{N_2}$ ) generally determines the sensitivity of  $a_{mix}$  toward the mixture properties. In our case, this spread is beyond  $100 \text{ m s}^{-1}$  for all

$T_{inj}$ , which will allow to discuss mixing characteristics on basis of the obtained LITA data.

Figure 5 shows centerline measurements for varying  $T_{inj}$  at different axial positions. Here, error bars represent the double standard error of the mean (i.e. twice the sample standard deviation divided by the square root of the sample size). Hence, it visualizes the expected variation of the mean values due to the precision of the measurements as well as the parameter fluctuations inherent to a turbulent flow field Kuehner et al. (2010), Williams et al. (2014), Kiefer et al. (2008).

For a fixed  $x/D$ , the dependency between  $a_{meas}$  and  $T_{inj}$  is approximately linear as visualized by dashed trend lines for which  $a_{meas}$  increases with  $T_{inj}$ . Consistent slopes are found at all three  $x/D$ -positions with an average increase in  $a$  of  $\approx 30 \text{ m s}^{-1}$  from  $T_{inj} = 554$  to  $630$  K. It is attributed to, firstly, a higher initial  $a_{hex}$  for higher  $T_{inj}$  (see Table 2) and, secondly, the lower initial jet momentum due to a decreasing density of the injectant with  $T_{inj}$ . The latter results in a reduced mass fraction of *n*-hexane ( $c_{hex,cl}$ ) as the entrainment of N<sub>2</sub> is promoted (Pitts 1991). Analogously, the axial increase of  $a_{meas}$  in Fig. 5 stems from progressing entrainment of N<sub>2</sub> along the jet centerline.

In addition to the centerline data, Fig. 6 illustrates radial distributions of  $a_{meas}$  at  $x/D = 55$  and  $80$  for  $T_{inj} = 554$  and  $630$  K. At both  $x/D$ , distinct minima are found at  $y/D = 0$  that can be related to a maximum  $c_{hex}$ . In radial direction,  $a_{meas}$  converges to  $a_{N_2} \approx 350 \text{ m s}^{-1}$  for large  $y/D$ . It results from the radial profile of the jet as  $\underline{c}$  and  $T$  approach the chamber condition and, hence, the properties of cold N<sub>2</sub>. For all profiles, an inverse bell shape is observed, although less pronounced at  $x/D = 80$  due to the lower spatial resolution in vicinity of the jet centerline. More importantly, however, the data in Fig. 6 feature the same trends

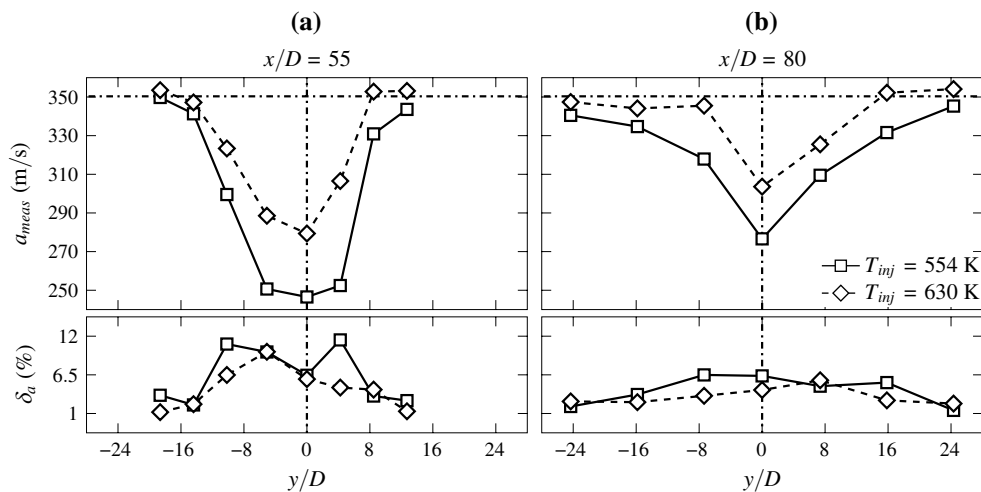


**Fig. 6** Radial distributions of  $a_{meas}$  at  $x/D = 55$  and  $80$  including the corresponding  $\delta_a$

as observed for the centerline. Higher  $T_{inj}$  increases  $a_{meas}$  at fixed  $x/D$  as it is also the case for an increase of  $x/D$  at constant  $T_{inj}$ . This, again, demonstrates the consistency of the presented data sets.

In an attempt to provide a more representative measure for the flow field fluctuations, single-shot variations in  $a_{meas}$  at the same condition have been calculated for the radial profiles and included in Fig. 6. They can be expressed in terms of the relative variation  $\delta_a = a_{RMSD}/\bar{a}_{meas}$ , where  $a_{RMSD}$  is the root-mean-square deviation and  $\bar{a}_{meas}$  the sample mean value. On average, 14 LITA signals were available to calculate  $\delta_a$ . As already discussed for Fig. 5, the variation magnitude convolutes the performance of the technique and the fluctuational nature of the flow field, whereas the latter dominates for highly turbulent mixing flows as studied here. Based on the considerations in Sect. 2.2.3, it is estimated that the contribution of the technique's precision to the overall variation in the measurement is approximately 2–3 %, whereas larger values are seen as feature of the flow field.

In fact, the relative variation is within the precision range for the radial outer jet domain, where  $a_{meas} \approx a_{N_2}$ . Approaching the shear layer region toward the jet inner core, where highly turbulent mixing is present,  $\delta_a$  increases significantly above the LITA uncertainty. For our experiments, values of up to 12 % are found for the position at  $x/D = 55$  indicating considerable flow field fluctuations. The same trend for  $\delta_a$  can be identified at  $x/D = 80$ , whereas the maximum value reduces to  $\approx 6.5$  %. This implies a more developed flow field at this position in which the impact of turbulent mixing diminishes.

To allow for an assessment of the obtained signal quality, representative LITA signals are shown in Fig. 7 for  $T_{inj} = 554$  K and  $x/D = 55$ . Here, implications of the

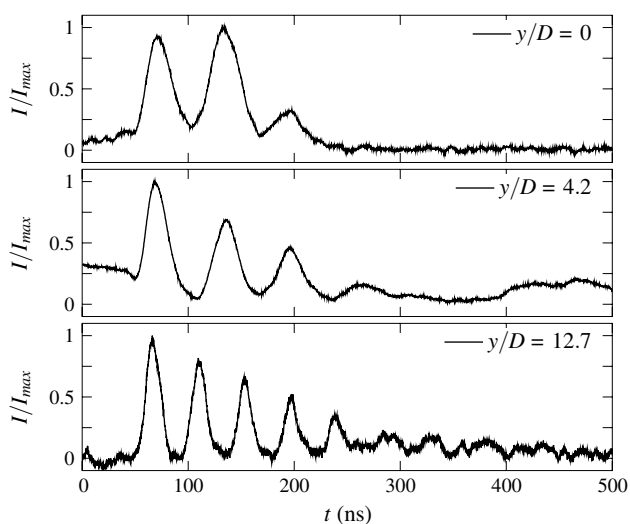


**Fig. 7** Normalized LITA signals for  $T_{inj} = 554$  K and  $x/D = 55$

different flow field regions can be identified. In case of  $y/D = 0$  and 4.2, the measurement volume penetrates regions of pronounced turbulent mixing characterized by high shear rates, especially considering the small spatial scale of the jet. Besides the inherent fluctuations, distortion of the fringe pattern (see Sect. 2.2.3) leads to elevated variation among the samples. Only three oscillations are present here. Furthermore, a nonzero signal intensity after complete grating dissipation can be identified, which is caused by beam steering effects. Nevertheless, characteristic signal periods can still be found even for irregularly shaped signals (see e.g.  $y/D = 0$ ) that deviate from those taken in laboratory environments as a consequence of the highly turbulent flow. This is corroborated by the consistent speed of sound profile shown in Fig. 6 and demonstrates that an actual LITA signal and not random noise is detected.

For the radial outer jet region, more oscillations are usually processable as it is visible for the signal at  $y/D = 12.7$ . In this context, it should also be noted that *n*-hexane acts as a molecular seeder due to its (weak) absorption around 1064 nm. Therefore, absolute signal intensities (i.e. signal-to-noise ratios) decrease with a reduction of  $c_{hex}$ . In fact, nonresonant grating excitation in pure  $N_2$  (i.e.  $c_{hex} = 0$ ) yielded no detectable intensities for the used laser settings. This also implies that data were always taken within the jet domain with at least residual  $c_{hex}$ .

## 4.2 Mixing characterization

Comparable studies found in the literature typically analyze the jet mixing process in terms of concentration and temperature. Speed of sound data provides information on both quantities, but only under assumption of a thermodynamic model to isolate the individual contributions. In the following, an adiabatic mixing model is presented that accounts for nonideality in the thermodynamic properties. Subsequently, this model is applied to experimental speed of sound data from Sect. 4.1 to characterize the mixture formation.

### 4.2.1 Adiabatic mixing model

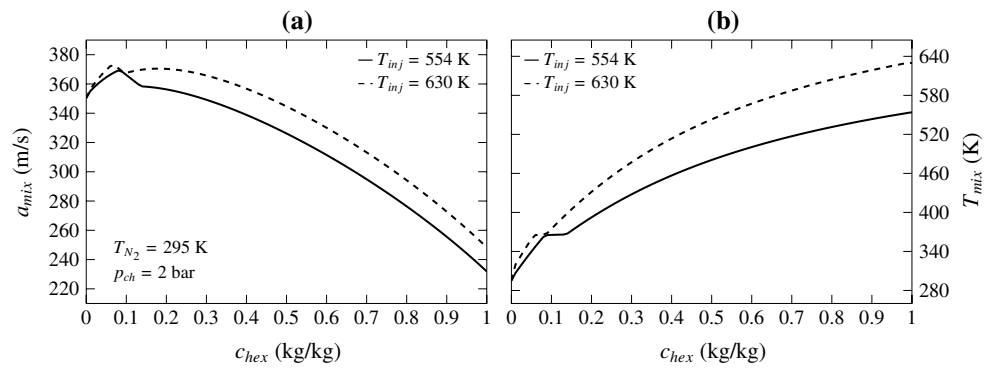
To determine  $c$  and  $T$  based on  $a_{meas}$ , the ambiguity of  $a_{meas}$  in these quantities is bypassed via an adiabatic mixing assumption of injectant and ambient gas. The specific enthalpy  $h_{mix}(c, T_{mix}, p_{ch})$  of a real mixture with adiabatic mixing temperature  $T_{mix}$  can then be written as

$$h_{mix}(c, T_{mix}, p_{ch}) - h_{excess}(c, T_{mix}, p_{ch}) = h_{id}(c, T_{mix}, p_{ch}). \quad (3)$$

Here,  $h_{id}$  is the specific enthalpy for an ideal mixing of *n*-hexane and  $N_2$ , while  $h_{excess}$  accounts for nonideality of the binary system. As discussed in Sect. 3, the expansion of *n*-hexane to  $p_{ch}$  leads to  $T_{ps} = T_{inj}$  prior to mixing. Nitrogen, on the other hand, is at  $T_{ch}$  and  $p_{ch}$ . It follows that



**Fig. 8** Speed of sound and temperature for adiabatic mixing of *n*-hexane and N<sub>2</sub> at  $p_{ch} = 2$  bar



$$h_{id}(\underline{c}, T_{ps}, T_{ch}, p_{ch}) = \dots \dots c_{hex} h_{hex}(T_{ps}, p_{ch}) + (1 - c_{hex}) h_{N_2}(T_{ch}, p_{ch}), \quad (4)$$

where  $h_{hex}$  and  $h_{N_2}$  are the pure (pressure-dependent) specific enthalpies. Based on NIST REFPROP (Lemmon et al. 2013) data for  $a_{mix}$  and all  $h_i$ , an iterative scheme optimizes for  $\underline{c}$  and  $T_{mix}$  so that

$$a_{mix}(\underline{c}, T_{mix}, p_{ch}) \stackrel{!}{=} a_{meas}, \quad (5)$$

while at the same time

$$h_{mix}(\underline{c}, T_{mix}, p_{ch}) - h_{excess}(\underline{c}, T_{mix}, p_{ch}) \stackrel{!}{=} \dots \dots c_{hex} h_{hex}(T_{ps}, p_{ch}) + (1 - c_{hex}) h_{N_2}(T_{ch}, p_{ch}). \quad (6)$$

It must be stressed that this approach yields an approximation of  $\underline{c}$  and  $T_{mix}$ . However, the proposed procedure is not limited to the assumption of ideal gases and can be seen as an extension to models typically used for Rayleigh (Idicheria and Pickett 2007) and LIF (Gamba et al. 2015) measurements. In fact, real fluid behavior is provided using the NIST database. The binary *n*-hexane/N<sub>2</sub> mixture is described by an EOS developed by Kunz and Wagner (2012). Hence, the developed approach is generally valid for nonideal mixing provided that thermodynamic transport processes such as diffusion and heat conduction are negligible, which is true for a wide range of conditions including the ones considered here. By satisfying Eqs. (5) and (6), it is, therefore, possible to analyze the experimental speed of sound data with respect to the mixture behavior. The general relation between  $a_{mix}$ ,  $T_{mix}$  and  $c_{hex}$  is illustrated in Fig. 8. As can be deduced from Fig. 8a,  $a_{mix}$  is nonmonotonic within  $0 \leq c_{hex} \leq 1$ . For low  $c_{hex}$ , the speed of sound increases to values above  $a_{N_2}$ , whereas the altering course in  $a_{mix}$  for  $c_{hex} < 0.1$  is due to the entrance into the two-phase region of the mixture. For  $c_{hex} > 0.2$ ,  $a_{mix}$  features monotonic decrease down to  $a_{hex}(T_{inj})$  at  $c_{hex} = 1$ . A unique nonlinear function in  $c_{hex}$  is, hence, obtained for  $a_{mix} < 350 \text{ m s}^{-1}$ , which assures a distinct determination of  $c_{hex}$ . Note that the majority of  $a_{meas}$  from Figs. 5 and 6

fulfill this criterion. In Fig. 8b, the corresponding  $T_{mix}$  is illustrated featuring monotonic increase in  $c_{hex}$  (apart from the two-phase region).

#### 4.2.2 Centerline concentration

According to a similarity law proposed by Chen and Rodi (1980), the axial concentration decay for momentum-controlled mixing is described by

$$c_{cl} = A \left( \frac{\rho_e}{\rho_{ch}} \right)^{0.5} \left( \frac{x}{D} \right)^{-1}. \quad (7)$$

Here,  $A$  is an empirical scaling constant,  $\rho_e$  the injectant density at the nozzle exit plane and  $\rho_{ch}$  the ambient gas density. Even though originally proposed for expanded jets, Molkov (2012) used Eq. (7) to collapse experimental concentration data for both expanded and underexpanded nonideal hydrogen jets at high pressures. The author shows that  $A = 5.4$  is suitable for a very wide range of experimental conditions (i.e. pressure ratio, nozzle diameter, axial distance). In the following, the correlation is applied to the present experiments to assess whether it also holds for underexpanded jets with near-critical reservoir temperature injected into a low-pressure atmosphere.

The adiabatic mixing approach was used to determine centerline concentrations for the conditions in Table 1, which are illustrated in Fig. 9a. An axial concentration decay can be identified, whereas higher  $T_{inj}$  also lead to lower  $c_{hex,cl}$  at a given  $x/D$ . Note that these trends are consistent with the interpretation of  $a_{meas}$  in Figs. 5 and 6. The characteristic of  $c_{hex,cl}$  is well described by the similarity law in Eq. (7), which holds for both the axial decay as well as the influence of  $T_{inj}$ . In addition to our data, measurements from Wu et al. (1999) are included in Fig. 9. Using Raman scattering, they obtained quantitative concentration data for ethylene jets injected into N<sub>2</sub>. As summarized in Table 3, comparable conditions were investigated resulting in extremely underexpanded jets at near-critical injection temperature as well.

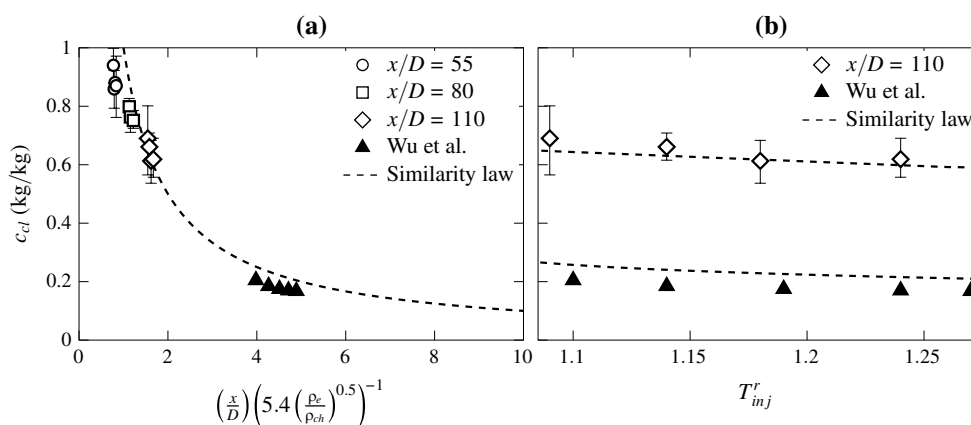


**Fig. 9** Similarity analysis of  $c_{cl}$  for  $n$ -hexane and ethylene injections (error bars represent the double standard error of the sample mean)

**Table 3** Overview of experimental conditions considered in Fig. 9

Study	Fuel/gas	$T_{inj}^r$	$p_{inj}^r$	$T_e^r$	$p_e^r$	$\rho_e$ ( $\frac{\text{kg}}{\text{m}^3}$ )	$T_{ch}$ (K)	$p_{ch}$ (bar)	$x/D$
Wu et al. (1999)	$\text{C}_2\text{H}_4/\text{N}_2$	1.10–1.27	1.2	0.97–1.13	$\approx 0.7$	41–61	300	2	112
Here	$\text{C}_6\text{H}_{14}/\text{N}_2$	1.09–1.24	9.9	1.05–1.20	2.7–4.1	340–397	295	2	110

With respect to Fig. 9a, these data represent a different regime of the similarity law. While our data are located in the fast decay region associated with high initial injectant concentrations, the overall evolution of the similarity law is corroborated by the data of Wu et al. (1999). Hence, it provides a good approximation also for underexpanded jets at near-critical injection temperature and different fluid types.

A direct comparison of the two data sets at approximately the same  $x/D$  (see Table 3) is provided in Fig. 9b. Note that, although  $T_{inj}^r$  is comparable, a three times higher  $c_{cl}$  is found in this work that is, however, well predicted by the similarity law. As  $x/D$  and  $\rho_{ch}$  are equal in both experiments,  $\rho_e$  remains the only scaling factor for  $c_{cl}$  (see Eq. 7). In Fig. 4 it was already shown that  $n$ -hexane exits as a supercritical fluid in our experiments, which is accompanied by liquid-like densities of up to  $400 \text{ kg m}^{-3}$  at the nozzle exit plane. On the contrary, the jets of Wu et al. are expanded into the vapor regime with  $p_e^r < 1$  resulting in considerably lower  $\rho_e$  ( $\approx 60 \text{ kg m}^{-3}$ ). Therefore, it is the difference in  $\rho_e$  that leads to the significantly varying fuel concentrations in both data sets.

It can be concluded that the relevant thermodynamic regime for the expansion process within the nozzle has high impact on the farfield injectant concentration for supercritical reservoir conditions. Particularly within the transition region from a supercritical fluid ( $p_e^r > 1$  and  $T_e^r > 1$ ) to the subcritical vapor domain ( $p_e^r < 1$  and  $T_e^r > 1$ ) for the nozzle exit condition, large gradients in  $\rho_e$  (see Fig. 4) may strongly influence the mixing characteristics as it is

demonstrated by the comparison of both data sets. For valid mixture prediction, it is, therefore, mandatory to provide an accurate nonideal EOS to describe the expansion process within the nozzle (see Sect. 3). The farfield jet mixing at high, possibly supercritical, temperature and subcritical pressure can be treated as adiabatic and is well described by the similarity law in Eq. (7), without the necessity to characterize the complex expansion process from nozzle exit to Mach disk.

#### 4.2.3 Radial profiles

As the evolution of  $c_{cl}$  follows a similarity law, self-preserving behavior may also be present for the radial jet temperature and concentration distribution. This is generally true for the farfield zone, where the turbulent flow is fully developed (Richards and Pitts 1993). Our motivation is, therefore, to assess whether the experimental speed of sound data in Fig. 6 can be reproduced under the assumption of self-similarity in  $c$  and  $T$ . The procedure for this is as follows:

- Assumption of normalized Gaussian distributions for the radial  $c$  and  $T$  profiles.
- Calculation of  $c_{cl}$  and  $T_{cl}$  from  $a_{meas}(y/D = 0)$  using the adiabatic mixing approach.
- Calculation of radial speed of sound profiles from EOS based on Gaussian  $c$  and  $T$  distributions scaled with  $c_{cl}$  and  $T_{cl}$ .

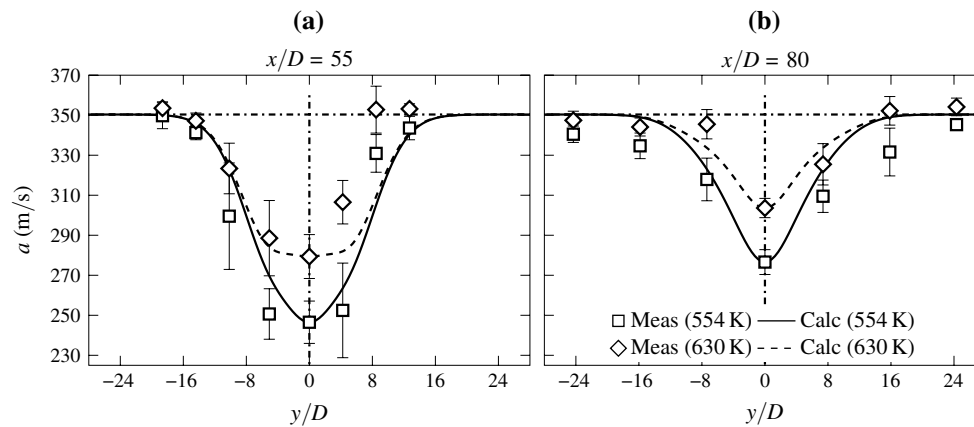


**Fig. 10** Comparison of measured and calculated radial speed of sound profiles (error bars represent the double standard error of the sample mean)

- Comparison of calculated and measured speed of sound profiles.

For the radial temperature profile in the farfield of an underexpanded jet, Yüceil and Ötügen (2002) suggest the scaling law

$$\frac{T_{\text{ch}} - T}{T_{\text{ch}} - T_{\text{cl}}} = 0.25^{(y/b_v)^2}, \quad (8)$$

where  $b_v = 0.095x$  is the jet velocity half-width.

A similar expression is found by Wu et al. (1999) for a self-preserving concentration characteristic according to

$$\frac{c}{c_{\text{cl}}} = \exp(-y^2/k^2), \quad (9)$$

where  $k$  is an empirical scaling constant specific to the topology of the jet under study. For the present work,  $k = 1.75$  was found as best representation of the experimental data.

At this stage, Eqs. (8) and (9) provide nondimensional profiles for  $c$  and  $T$ . In the next step, these profiles are scaled with the centerline values obtained by the adiabatic mixing model (see Sect. 4.2.1) resulting in absolute profiles in  $c$  and  $T$ . The last step is to calculate the radial speed of sound distribution on basis of these profiles and the EOS from NIST.

The comparison between measured and calculated speed of sound is shown in Fig. 10. Here, it is important to note that only the centerline value for  $a_{\text{calc}}$  is directly dictated by the measurement. The radial distribution, however, solely results from the real fluid property data in combination with the self-similarity assumption in  $c$  and  $T$ . Note also that these assumptions do not necessarily lead to a Gaussian profile in the speed of sound distribution. Actually, a different shape is observed in Fig. 10 for  $a_{\text{calc}}$  even though  $c$  and  $T$  are fixed to be

Gaussian. Keeping this in mind, it is clear that the good agreement of  $a_{\text{meas}}$  and  $a_{\text{calc}}$  at  $x/D = 55$  for both  $T_{\text{inj}}$  is not trivial, but corroborates that the assumed radial profiles for  $c$  and  $T$  are in fact reasonable approximations of the flow field.

The same also applies to the position further downstream at  $x/D = 80$ . Although larger deviations between calculated and measured profiles are found here, the agreement is still acceptable under the aforementioned aspects. The data in Fig. 10, furthermore, demonstrate the small-scale capability of LITA to yield quantitative speed of sound data with a discretization of approximately 1 mm ( $\approx 4D$ ), even when challenging aerodynamic conditions are present.

## 5 Conclusion

In this paper, we investigated extremely underexpanded  $n$ -hexane jets with supercritical reservoir condition injected into subcritical nitrogen atmosphere. To the authors knowledge, it is the first time that the nonintrusive measurement technique laser-induced thermal acoustics is demonstrated for highly turbulent mixing zones with nonuniform temperature and concentration field. Quantitative speed of sound data are presented for different supercritical injection temperatures and three axial positions. Additionally, consistent radial profiles with approximately 1 mm discretization ( $\approx 4$  nozzle diameters) were acquired showing the techniques suitability for small-scale phenomena. The effect of turbulent mixing on the jet disintegration is quantified by relative variations in the speed of sound as high as 12 % for the inner jet core. Using an adiabatic mixing model based on nonideal fluid properties, a quantitative database for local mixture compositions is presented. Complementing the latter by the existing literature data leads to a similarity law

for centerline concentration prediction. Furthermore, the experimental speed of sound data suggests self-preservation characteristics in concentration and temperature also in radial direction. It is found that the mixing characteristics for extremely underexpanded jets with supercritical reservoir condition are strongly influenced by the thermodynamic regime relevant for the expansion process within the nozzle. Particularly for the nozzle exit condition, transition from supercritical (high-density) fluid to subcritical vapor induces strong variation in the fuel concentrations. A one-dimensional isentropic treatment of the nozzle flow yields a good approximation of the nozzle exit condition provided that an accurate nonideal equation of state is used. The far-field mixing is then well characterized by the calculated exit density of the fuel and the proposed similarity law without necessity to characterize the complex thermodynamic process of the expansion from the nozzle exit to the Mach disk.

**Acknowledgments** This work was performed within the Collaborative Research Center “Technological foundations for the design of thermally and mechanically highly loaded components of future space transportation systems (SFB-TRR40).” The authors would like to thank the German Research Foundation (Deutsche Forschungsgemeinschaft) for the financial support of this work.

## References

- Antiescu G, Tavlarides LL, Geana D (2009) Phase transitions and thermal behavior of fuel-diluent mixtures. *Energy Fuels* 23(6):3068
- Baab S, Lamanna G, Weigand B (2014) Combined elastic light scattering and two-scale shadowgraphy of near-critical fuel jets. In: ILASS Americas 26th annual conference on liquid atomization and spray systems, Portland, OR
- Birch AD, Hughes DJ, Swaffield F (1987) Velocity decay of high pressure jets. *Combust Sci Technol* 52(1–3):161
- Borghesi G, Bellan J (2015) A priori and a posteriori investigations for developing large eddy simulations of multi-species turbulent mixing under high-pressure conditions. *Phys Fluids* 27(3):035117
- Bougie B, Tulej M, Dreier T, Dam N, Ter Meulen J, Gerber T (2005) Optical diagnostics of diesel spray injections and combustion in a high-pressure high-temperature cell. *Appl Phys B* 80(8):1039
- Chai N, Kulatilaka W, Naik S, Laurendeau N, Lucht R, Kuehner J, Roy S, Katta V, Gord J (2007) Nitric oxide concentration measurements in atmospheric pressure flames using electronic-resonance-enhanced coherent anti-Stokes Raman scattering. *Appl Phys B* 88(1):141
- Chen CJ, Rodi W (1980) Vertical turbulent buoyant jets: a review of experimental data. Pergamon Press, Oxford
- Dahms RN, Oefelein JC (2015) Liquid jet breakup regimes at supercritical pressures. *Combust Flame* 162(10):3648
- Edwards T (1993) USAF supercritical hydrocarbon fuels interests. In: 31st aerospace sciences meeting and exhibit, Reno, NV, 11–14 Jan 1993. AIAA paper 93-0807
- Espey C, Dec JE, Litzinger TA, Santavicca DA (1997) Planar laser Rayleigh scattering for quantitative vapor-fuel imaging in a diesel jet. *Combust Flame* 109(1):65
- Ewan BCR, Moodie K (1986) Structure and velocity measurements in underexpanded jets. *Combust Sci Technol* 45(5–6):275
- Falgout Z, Rahm M, Sedarsky D, Linne M (2016) Gas/fuel jet interfaces under high pressures and temperatures. *Fuel* 168:14
- Förster FJ, Baab S, Lamanna G, Weigand B (2015) Temperature and velocity determination of shock-heated flows with non-resonant heterodyne laser-induced thermal acoustics. *Appl Phys B* 121(3):235
- Franquet E, Perrier V, Gibout S, Bruel P (2015) Free underexpanded jets in a quiescent medium: a review. *Prog Aerosp Sci* 77:25
- Gamba M, Miller VA, Mungal MG, Hanson RK (2015) Temperature and number density measurement in non-uniform supersonic flowfields undergoing mixing using toluene PLIF thermometry. *Appl Phys B* 120(2):285
- Grünefeld G, Beushausen V, Andresen P, Hentschel W (1994) Spatially resolved raman scattering for multi-species and temperature analysis in technically applied combustion systems: spray flame and four-cylinder in-line engine. *Appl Phys B* 58(4):333
- Harstad K, Bellan J (2006) Global analysis and parametric dependencies for potential unintended hydrogen-fuel releases. *Combust Flame* 144(1):89
- Idicheria CA, Pickett LM (2007) Quantitative mixing measurements in a vaporizing diesel spray by rayleigh imaging. Technical report, SAE Technical Paper
- Kiefer J, Kozlov DN, Seeger T, Leipertz A (2008) Local fuel concentration measurements for mixture formation diagnostics using diffraction by laser-induced gratings in comparison to spontaneous Raman scattering. *J Raman Spectrosc* 39(6):711
- Kuehner JP, Tessier FA Jr, Kisoma A, Flittner JG, McErlean MR (2010) Measurements of mean and fluctuating temperature in an underexpanded jet using electrostrictive laser-induced gratings. *Exp Fluids* 48(3):421
- Kunz O, Wagner W (2012) The GERG-2008 wide-range equation of state for natural gases and other mixtures: an expansion of GERG-2004. *J Chem Eng Data* 57(11):3032
- Lemmon EW, Huber ML, McLinden MO (2013) NIST standard reference database 23: reference fluid thermodynamic and transport properties-REFPROP version 9.1. REFPROP Version 9.1, National Institute of Standards and Technology, Standard Reference Data Program, Gaithersburg
- Molkov V (2012) Hydrogen safety engineering: the state-of-the-art and future progress. Elsevier, Oxford
- Payri F, Pastor J, Pastor J, Julia J (2006) Diesel spray analysis by means of planar laser-induced exciplex fluorescence. *Int J Engine Res* 7(1):77
- Pitts W (1991) Effects of global density ratio on the centerline mixing behavior of axisymmetric turbulent jets. *Exp Fluids* 11:125
- Richards CD, Pitts WM (1993) Global density effects on the self-preservation behaviour of turbulent free jets. *J Fluid Mech* 254(1):417
- Roshani B, Flägel A, Schmitz I, Kozlov DN, Seeger T, Zigan L, Kiefer J, Leipertz A (2013) Simultaneous measurements of fuel vapor concentration and temperature in a flash-boiling propane jet using laser-induced gratings. *J Raman Spectrosc* 44(10):1356
- Schlamp S, Sobota T (2002) Measuring concentrations with laser-induced thermalization and electrostriction gratings. *Exp Fluids* 32(6):683
- Seeger T, Jonuscheit J, Schenk M, Leipertz A (2003) Simultaneous temperature and relative oxygen and methane concentration measurements in a partially premixed sooting flame using a novel cars-technique. *J Mol Struct* 661:515
- Seeger T, Kiefer J, Weikl MC, Leipertz A, Kozlov DN (2006) Time-resolved measurement of the local equivalence ratio in a gaseous propane injection process using laser-induced gratings. *Opt Express* 14(26):12994

- Segal C, Polikhov S (2008) Subcritical to supercritical mixing. *Phys Fluids* 20(5):052101
- Span R, Wagner W (2003) Equations of state for technical applications. II. Results for nonpolar fluids. *Int J Thermophys* 24(1):41
- Stotz I (2011) Shock tube study on the disintegration of fuel jets at elevated pressures and temperatures. Ph.D. thesis, University of Stuttgart
- Su L, Helmer D, Brownell C (2010) Quantitative planar imaging of turbulent buoyant jet mixing. *J Fluid Mech* 643:59
- Taschek M, Egermann J, Schwarz S, Leipertz A (2005) Quantitative analysis of the near-wall mixture formation process in a passenger car direct-injection diesel engine by using linear Raman spectroscopy. *Appl Opt* 44(31):6606
- Tavlarides LL, Antiescu G (2009) Supercritical diesel fuel composition, combustion process and fuel system. US Patent 7,488,357
- Tedder SA, Weigl MC, Seeger T, Leipertz A (2008) Determination of probe volume dimensions in coherent measurement techniques. *Appl Opt* 47(35):6601
- Van Cruyningen I, Lozano A, Hanson RK (1990) Quantitative imaging of concentration by planar laser-induced fluorescence. *Exp Fluids* 10(1):41
- Weigl MC, Beyrau F, Kiefer J, Seeger T, Leipertz A (2006) Combined coherent anti-Stokes Raman spectroscopy and linear Raman spectroscopy for simultaneous temperature and multiple species measurements. *Opt Lett* 31(12):1908
- Williams B, Edwards M, Stone R, Williams J, Ewart P (2014) High precision in-cylinder gas thermometry using laser induced gratings: quantitative measurement of evaporative cooling with gasoline/alcohol blends in a GDI optical engine. *Combust Flame* 161(1):270
- Wolff M, Delconte A, Schmidt F, Gucher P, Lemoine F (2007) High-pressure diesel spray temperature measurements using two-colour laser-induced fluorescence. *Meas Sci Technol* 18(3):697
- Wu PK, Chen TH, Nejad AS, Carter CD (1996) Injection of supercritical ethylene in nitrogen. *J Propuls Power* 12(4):770
- Wu PK, Shahnam M, Kirkendall KA, Carter CD, Nejad AS (1999) Expansion and mixing processes of underexpanded supercritical fuel jets injected into superheated conditions. *J Propuls Power* 15(5):642
- Yüceil KB, Ötügen MV (2002) Scaling parameters for underexpanded supersonic jets. *Phys Fluids* 14(12):4206